A High-Pass Phase Plate Design for OMEGA and the NIF

Introduction

The direct-drive configuration utilized in inertial confinement fusion (ICF)[1,2] driven by high-powered lasers requires target illumination with a high degree of uniformity, especially in the lower spatial-frequency modes. Nonuniformity in laser irradiation seeds the Rayleigh–Taylor hydrodynamic instability, which consequently degrades target performance.[3–9] Various techniques, such as two-dimensional (2-D) smoothing by spectral dispersion (SSD),[10–13] distributed phase plates (DPP's),[14,15] polarization smoothing (PS),[16–22] and multiple beam overlap, are employed on the OMEGA laser[16,23,24] and will be employed on the National Ignition Facility (NIF) to improve the on-target irradiation uniformity and reduce the laser imprint. The nonuniformity in the lower frequencies (or spherical-harmonic ℓ modes) is particularly dangerous in ICF implosions due to hydrodynamic instabilities that develop during the longer imprinting periods associated with these modes. In addition, these low-order modes are also the most difficult to smooth with the aforementioned methods.

Reduced-autocorrelation phase plates were proposed to reduce the power spectrum of the low-ℓ modes and were designed with discrete phase elements of fixed spatial aperture.[25] These phase plates were calculated by changing selected phase elements in order to minimize the local autocorrelation function of the near-field phase term; hence the name. The reduced-autocorrelation phase plates, calculated by this method, were able to reduce the nonuniformity in the lower-ℓ modes by only a modest average factor of 2 without any near-field phase aberrations. In addition, due to the discrete nature of the phase plate elements, the envelope of the far-field intensity pattern was not controllable (except by changing the shape/size of the discrete phase elements).

The novel and improved design technique presented in this article calculates continuous versions of these specialized phase plates by directly manipulating the power spectrum of the far-field intensity pattern. These new designs are dubbed "high-pass phase plates" to distinguish them from their predecessors and to emphasize the method of directly manipulating the spectrum. The novel phase plate design technique calculates continuous phase plates that produce well-defined far-field intensity envelopes with a high degree of azimuthal symmetry and a controllable power spectrum. The high-pass phase plates are able to reduce the nonuniformity in the lower-ℓ modes by average factors of 4 to 10 (depending on the type of high-pass filter employed) without any near-field phase aberrations. The novel plate design technique presented can also be applied to standard phase plates because it requires no control of the far-field power spectrum. In addition, this technique is computationally efficient, and the calculation speeds are improved by two orders of magnitude over current methods.

The performance of high-pass phase plates is significantly affected by any near-field phase aberrations present on a high-powered ICF laser beam. If the phase aberration is strong enough, the resultant far-field intensity's power spectrum tends toward that produced by a standard continuous phase plate. Simulations of the far-field intensity pattern with applied phase aberrations (either measured or simulated), using the code *Waasikwa'*,[24] shows that the lower-ℓ-mode range can still benefit from these high-pass phase plates. High-pass phase plate designs for both OMEGA and the NIF can realize a reduction of about a factor of $\sqrt{2}$ to 2 in nonuniformity over the lower-ℓ-band range ($11 \le \ell \le 25$) in the presence of typical laser system phase aberrations.

In the following sections, an overview of the novel phase plate design technique will be presented. Next, standard phase plate designs will be compared to high-pass designs for both OMEGA and the NIF. The affect of near-field phase aberrations will then be discussed followed by the improvement realized in the lower-ℓ-band range in the presence of near-field phase aberrations.

A Novel Phase Plate Design Technique

A novel phase plate design technique was developed to calculate continuous phase plates that produce a well-defined far-field intensity envelope with a high degree of azimuthal symmetry and a controllable power spectrum and is incorpo-

rated in a code called *Zhizhoo'*.[26] *Zhizhoo'* can be configured to calculate a continuous near-field phase plate that produces a speckled far-field spot who's envelope matches almost any well-behaved function and has the ability to control the power spectrum of the far-field intensity in order to produce a speckled pattern with reduced nonuniformity in the low-order modes. A phase plate that reduces the nonuniformity in the low-order modes is referred to as a high-pass phase plate. The technique is computationally efficient and can complete a calculation in 10 to 20 min running on an SGI Origin 2000 machine with eight parallel processors.

The goal of the novel phase plate design technique is to produce a diffractive phase optic that varies slowly across the whole beam aperture and possesses no sharp discontinuities or phase anomalies. Simulated annealing is the current technique used at LLE to calculate continuous phase plates, but it tends to be computationally inefficient and takes tens of hours to complete a calculation.[14,15] The novel phase plate design technique wraps an additional iterative process around a standard phase-retrieval technique that is able to control the spatial and spectral properties of the speckled far-field intensity pattern while calculating a continuous phase plate. Two user-supplied design functions drive the algorithms to produce the required phase plate: the near-field beam intensity $\left|E_0\left(x_{\mathrm{nf}}, y_{\mathrm{nf}}\right)\right|^2$ and the far-field intensity envelope target $I_{\mathrm{ff_{target}}}\left(x_{\mathrm{ff}}, y_{\mathrm{ff}}\right)$, where $\left(x_{\mathrm{nf}}, y_{\mathrm{nf}}\right)$ and $\left(x_{\mathrm{ff}}, y_{\mathrm{ff}}\right)$ are the near-field and far-field coordinate systems, respectively.

1. Standard Phase-Retrieval Technique

The core or central algorithm of the novel phase plate design technique presented here is based on a standard phase-retrieval technique known as the error-reduction scheme; the error is guaranteed to never increase after every iteration.[27,28] The standard phase-retrieval algorithm employs the property of Fourier optics that connects the complex near- and far-field quantities via the Fourier transform,[29] where the far field is at the focal plane of the final lens in the long laser chain in OMEGA and the NIF, viz.,

$$\tilde{E}\left(x_{\mathrm{ff}}, y_{\mathrm{ff}}\right) = \iint E\left(x_{\mathrm{nf}}, y_{\mathrm{nf}}\right) \exp\left\{-i\frac{2\pi}{\lambda_{\mathrm{UV}} f}\left[x_{\mathrm{ff}} x_{\mathrm{nf}} + y_{\mathrm{ff}} y_{\mathrm{nf}}\right]\right\} dx_{\mathrm{nf}}\, dy_{\mathrm{nf}} = \Im\left\{E\left(x_{\mathrm{nf}}, y_{\mathrm{nf}}\right)\right\}, \tag{1}$$

$$E\left(x_{\mathrm{nf}}, y_{\mathrm{nf}}\right) = \frac{1}{\left(\lambda_{\mathrm{UV}} f\right)} \iint \tilde{E}\left(x_{\mathrm{ff}}, y_{\mathrm{ff}}\right) \exp\left\{+i\frac{2\pi}{\lambda_{\mathrm{UV}} f}\left[x_{\mathrm{ff}} x_{\mathrm{nf}} + y_{\mathrm{ff}} y_{\mathrm{nf}}\right]\right\} dx_{\mathrm{ff}}\, dy_{\mathrm{ff}} = \Im^{-1}\left\{\tilde{E}\left(x_{\mathrm{ff}}, y_{\mathrm{ff}}\right)\right\}, \tag{2}$$

where λ_{UV} = 351 nm is the UV laser wavelength, f is the focal length of the final focusing lens (f = 1.8 m for OMEGA and f = 7.7 m for the NIF), and operators $\Im\{.\}$ and $\Im^{-1}\{.\}$ define the 2-D spatial Fourier transform and its inverse, respectively, that map the complex-valued electric field from the near-field coordinates $\left(x_{\mathrm{nf}}, y_{\mathrm{nf}}\right)$ to the far-field coordinates $\left(x_{\mathrm{ff}}, y_{\mathrm{ff}}\right)$ and vice versa. The magnitudes of the near-field or input beam shape

$$E_0\left(x_{\mathrm{nf}}, y_{\mathrm{nf}}\right) = \left|E\left(x_{\mathrm{nf}}, y_{\mathrm{nf}}\right)\right| \tag{3}$$

and the speckled far-field objective pattern

$$\tilde{E}_0\left(x_{\mathrm{ff}}, y_{\mathrm{ff}}\right) = \left|\tilde{E}\left(x_{\mathrm{ff}}, y_{\mathrm{ff}}\right)\right| \tag{4}$$

are known *a priori* before the iterative procedure is initiated. During the iterative procedure, the known input beam shape replaces the calculated amplitude of the near field and the far-field objective pattern replaces the calculated amplitude of the far field, while the calculated phase of both complex fields is retained.[28] A diagram of this iterative procedure is illustrated in Fig. 89.10. This algorithm converges quickly and accurately to almost any desirable far-field envelope; the main restrictions are that the envelope be square integrable and possess no sharp discontinuities, i.e., a well-behaved function.[31] The phase calculated during this standard technique is bounded by $\pm\pi$ due to the inherent range of the *arctangent* function used to calculate the phase based on the real and imaginary parts of the complex field quantities.

Bounding the phase in this manner results in many sharp 2π-phase discontinuities that theoretically will not scatter energy; however, a realistic device will scatter energy out of the desired far-field envelope because this boundary is not exactly reproduced due to limitations in the manufacturing process.[32] The

standard phase-retrieval technique can also produce phase anomalies that have sharp π-phase discontinuities (accurately referred to as phase dislocations[33] or phase vortices and imprecisely called phase poles or spiral phase singularities), which scatter additional light when they are illuminated (because a field value of zero is expected at phase dislocations) and are not due to a manufacturing limitation, although manufacturing limitations can exacerbate the scatter. A π-phase discontinuity occurs independently of the direction that the phase dislocation is traversed,[31] and a total of 2π phase is accumulated on a line integral path encircling a phase dislocation of order 1.[34] Both of these scattering sources limit the usefulness of the standard phase technique.

The sharp 2π-phase discontinuities can be removed by a number of different phase-unwrapping algorithms.[35] The phase anomalies pose a much more insidious problem because not only do they inhibit many phase-unwrapping algorithms, they also are one of the main reasons that the standard phase-retrieval technique stagnates or fails to converge.[36] If one attempts to artificially remove the phase discontinuities, they will simply reappear later in another location during the standard phase retrieval's iteration process.[31] Using the standard phase-retrieval technique alone renders the phase dislocations irremovable.

The number of phase anomalies can be reduced by initializing the standard phase technique with distributions that do not inherently contain phase anomalies[34] (which can frequently occur in random distributions); however, some problems benefit equally as well from a random distribution.[36] Another method attempts to remove pairs of phase dislocations by smoothing over the region containing them and then restricting the degree of freedom in that region during further iterations. This method, however, results in a rather tedious and complicated algorithm that requires searching for and identifying pairs of phase dislocations that may not even reside on the current computational grid.[34]

Phase dislocations are associated with zeros of complex functions.[37–42] If a phase dislocation exists, a complex zero exists (although the opposite is not necessarily true). One source of phase dislocations in the near field is hard clipping or aggressive attenuation of the spatial spectrum (or far field).[31] If a near-field object's spectrum extends beyond the computational domain of the far field or extends into a region where the far-field target is zero, hard clipping can occur. Alternatively, aggressive attenuation of the spatial frequencies can occur during the application of the far-field constraints, i.e., applying a far-field target function that falls rapidly toward zero in regions where the near-field object's spectrum has significant values. Both of these mechanisms can occur when the near-field phase possesses large gradients, which will introduce complex zeros into the near field during the phase-retrieval procedure. It can also be shown, however, that if a near-field object has a spectrum with compact or finite support (i.e., a band-limited function), a near-field phase without phase dislocations can be found.[31]

2. Initial Guess and Construction of the Far-Field Objective

Both the standard phase retrieval and novel phase plate design techniques require an initial guess of the near-field phase. Through a judicious choice, the algorithms can be given a jump-start on convergence that helps prevent stagnation (as mentioned in the previous section). A random initial guess whose values take on any phase in the interval $0 \le \phi \le 2\pi$ can be a useful generic starting point for many applications where phase dislocations are not that much of a concern. This random pattern, however, is not a prudent starting point for continuous phase plate designs.

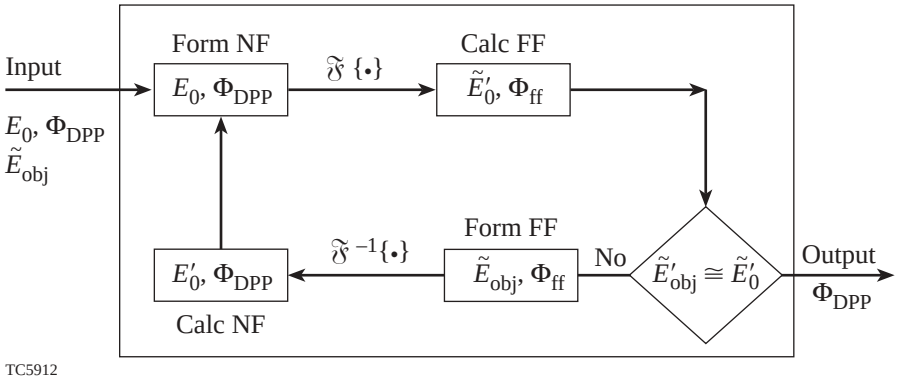

Figure 89.10
A flow diagram depicting the iterative process employed in the standard phase-retrieval technique. The idea behind this technique has a long history dating back to Wolf[30] in 1962. Gerchberg, Saxton, and Fienup extended this idea to two dimensions, and the basic error-reduction scheme is shown in this figure.[27,28] This iterative technique is at the core of the novel phase plate design technique.

The best choice for a continuous phase plate design is one whose phase is already continuous and produces a far-field pattern that adequately covers the targeted region. A scaled, colored-noise (see Carslon,[41] pp. 153–154) phase pattern is suitable for this purpose and is given by a Fourier filter operation:

$$\hat{\Phi}_{\mathrm{DPP}}(x_{\mathrm{nf}},y_{\mathrm{nf}}) = a\cdot\Re\left\{\Im^{-1}\left\{\Im\left\{\zeta(x_{\mathrm{nf}},y_{\mathrm{nf}})\right\}\right.\right.$$

$$\left.\left.\exp\left[-\ln(2)\cdot\left(\frac{k_{\mathrm{nf}}}{k_{0_{\mathrm{DPP}}}}\right)^{20}\right]\right\}\right\}, \qquad (5)$$

where a is the scaling constant, $\zeta(x_{\mathrm{nf}},y_{\mathrm{nf}})\in[-1,1]$ is a random number field, $k_{\mathrm{nf}}\equiv\left(k_{x_{\mathrm{nf}}}^2+k_{y_{\mathrm{nf}}}^2\right)^{1/2}$ is the radial wave number of the near-field coordinate system, $k_{0_{\mathrm{DPP}}}=360$ rad/m is the FWHM filter point, and $\Re\{\cdot\}$ is the real operator. When the color-noise phase pattern, given by Eq. (5), is used, the resultant far-field speckle pattern possesses a simple Gaussian envelope. The scaling constant a is used to effectively spread out the resultant far-field speckle pattern to cover the targeted area (the value used in this article is a = 50 rad for both OMEGA and the NIF). It is important for the constant a to be large enough to encompass the targeted area of the far field but not so large that it extends beyond the computational region of the far field (otherwise, aliasing effects can play havoc on the algorithm).

Once the initial phase $\hat{\Phi}_{\mathrm{DPP}}(x_{\mathrm{nf}},y_{\mathrm{nf}})$ is chosen, manipulating the initial speckled far-field pattern produced by the initial phase generates the first far-field objective pattern. The initial speckled far-field pattern is given by

$$\hat{\tilde{E}}_0(x_{\mathrm{ff}},y_{\mathrm{ff}}) = \left|\Im\left\{E_0(x_{\mathrm{nf}},y_{\mathrm{nf}})\cdot\exp\left\{i\hat{\Phi}_{\mathrm{DPP}}(x_{\mathrm{nf}},y_{\mathrm{nf}})\right\}\right\}\right|. \qquad (6)$$

First, the envelope of the initial speckled far-field intensity pattern is found by using an optimal filter technique (described in detail in the following section):

$$I_{\mathrm{ff}_{\mathrm{env}}}(x_{\mathrm{ff}},y_{\mathrm{ff}}) = \Re\left\{\Im^{-1}\left\{\tilde{\Psi}_{\mathrm{opt}}(k_{x_{\mathrm{ff}}},k_{y_{\mathrm{ff}}})\right.\right.$$

$$\left.\left.\Im\left\{\left|\hat{\tilde{E}}_0(x_{\mathrm{ff}},y_{\mathrm{ff}})\right|^2\right\}\right\}\right\}, \qquad (7)$$

where $\tilde{\Psi}_{\mathrm{opt}}(k_{x_{\mathrm{ff}}},k_{y_{\mathrm{ff}}})$ is the optimal filter. Next a transformation function $\Lambda(x_{\mathrm{ff}},y_{\mathrm{ff}})$ is defined as

$$\Lambda(x_{\mathrm{ff}},y_{\mathrm{ff}}) \equiv \begin{cases} \left[\dfrac{I_{\mathrm{ff}_{\mathrm{target}}}(x_{\mathrm{ff}},y_{\mathrm{ff}})}{I_{\mathrm{ff}_{\mathrm{env}}}(x_{\mathrm{ff}},y_{\mathrm{ff}})}\right]^{1/2} & ;\quad I_{\mathrm{ff}_{\mathrm{env}}}(x_{\mathrm{ff}},y_{\mathrm{ff}})\neq 0 \\ 0 & ;\quad \text{otherwise} \end{cases}, \qquad (8)$$

where $I_{\mathrm{ff}_{\mathrm{target}}}(x_{\mathrm{ff}},y_{\mathrm{ff}})$ is the far-field target intensity envelope. The function $\Lambda(x_{\mathrm{ff}},y_{\mathrm{ff}})$ transforms the initial far-field pattern as

$$\tilde{E}_{\mathrm{obj}}(x_{\mathrm{ff}},y_{\mathrm{ff}}) = \Lambda(x_{\mathrm{ff}},y_{\mathrm{ff}})\cdot\hat{\tilde{E}}_0(x_{\mathrm{ff}},y_{\mathrm{ff}}), \qquad (9)$$

where $\tilde{E}_{\mathrm{obj}}(x_{\mathrm{ff}},y_{\mathrm{ff}})$ yields the first speckled far-field objective based on the initial far-field pattern $\hat{\tilde{E}}_0(x_{\mathrm{ff}},y_{\mathrm{ff}})$. The importance of Eq. (9) is both subtle and critical to the convergence to a continuous phase plate; the initial phase $\hat{\Phi}_{\mathrm{DPP}}(x_{\mathrm{nf}},y_{\mathrm{nf}})$ is correlated to the generated speckle pattern. If this correlation is not maintained, convergence can be lost and the resultant phase pattern tends to produce a speckled far field with a Gaussian-shaped envelope and, under extreme cases, a high central peak develops. The transformation function $\Lambda(x_{\mathrm{ff}},y_{\mathrm{ff}})$ may contain anomalously high values where $I_{\mathrm{ff}_{\mathrm{env}}}(x_{\mathrm{ff}},y_{\mathrm{ff}})\sim 0$. These values are eventually suppressed during the enhancement procedure described in the next section.

3. Wrapper Algorithm: Phase Continuity and Convergence Enhancement

The continuity of the calculated phase is controlled using a two-step process: a 2-D phase-unwrapping procedure is applied to the phase map, calculated using the standard phase-retrieval method, followed by a low-pass filter that removes any residual high frequencies. The 2-D phase-unwrapping problem can be expressed in the form of Poisson's equation. The 2-D phase-unwrapping algorithm implemented in *Zhizhoo'* directly solves Poisson's equation on the whole computational grid using cosine transforms and does not need to painstakingly iterate around the grid as in other methods.[35] The cosine transform technique acts globally on the phase function and therefore is relatively immune to any local phase anomalies in that it tends to smooth over discontinuities, which is a highly desirable feature in the design of continuous phase plates.

Initially, when there are a number of phase anomalies, some residual high-frequency artifacts that remain after the 2-D phase-unwrapping operation need to be additionally smoothed. A simple, smooth, low-pass filter is used to remove the high-frequency artifacts, where the filter is a super-Gaussian:

$$\tilde{\Psi}_{\Phi}\left(k_{x_{\mathrm{nf}}},k_{y_{\mathrm{nf}}}\right)=\exp\left\{-\ln(2)\left(\frac{k_{\mathrm{nf}}}{k_{0_{\mathrm{DPP}}}}\right)^{20}\right\}, \tag{10}$$

where $k_{0_{\mathrm{DPP}}}=1270\ \mathrm{rad/m}$ is the FWHM filter point. Note that the filtering function used here is the same as that implemented in the initial guess of the phase except that the quantity $k_{0_{\mathrm{DPP}}}$ is larger. The filtering is implemented as

$$\Phi_{\mathrm{DPP}}\left(x_{\mathrm{nf}},y_{\mathrm{nf}}\right)=\Re\left\{\Im^{-1}\left\{\tilde{\Psi}_{\Phi}\left(k_{x_{\mathrm{nf}}},k_{y_{\mathrm{nf}}}\right)\Im\left\{\Phi'_{\mathrm{DPP}}\left(x_{\mathrm{nf}},y_{\mathrm{nf}}\right)\right\}\right\}\right\}, \tag{11}$$

where $\Phi'_{\mathrm{DPP}}\left(x_{\mathrm{nf}},y_{\mathrm{nf}}\right)$ is the unwrapped phase, $\Re\{\cdot\}$ is the real operator, and the coordinate transformations $k_{x_{\mathrm{nf}}}=2\pi x_{\mathrm{ff}}/\left(\lambda_{\mathrm{UV}}f\right)$ and $k_{y_{\mathrm{nf}}}=2\pi y_{\mathrm{ff}}/\left(\lambda_{\mathrm{UV}}f\right)$ are required to use the definitions in Eqs. (1) and (2).

The speckled far field must be recalculated to account for any changes that occur due to the updated phase plate $\Phi_{\mathrm{DPP}}\left(x_{\mathrm{nf}},y_{\mathrm{nf}}\right)$ after continuity is corrected by the unwrapping and filtering process. This speckled far field becomes the current speckled far-field objective and is represented as $\tilde{E}'_{\mathrm{obj}}\left(x_{\mathrm{ff}},y_{\mathrm{ff}}\right)$. At first, the resultant unwrapped and filtered phase mapping does not produce a speckled far-field pattern whose envelope matches the target envelope. The whole procedure is then repeated until the continuous phase mapping converges and produces the targeted far-field envelope or reaches a fixed number of iterations. A flow diagram of the complete *Zhizhoo'* design process including the standard phase-retrieval technique is illustrated in Fig. 89.11.

An additional feature is also implemented to encourage fast and accurate convergence before the whole wrapper algorithm is repeated; the far-field target objective is "enhanced" or "emphasized" to compensate for any shortcomings of the current phase mapping, i.e., any azimuthal asymmetries or spurious peaks and valleys in the current far-field intensity envelope are corrected by modifying the 2-D far-field objective to dampen the peak-to-valley variation. This idea is similar to the input/output algorithm described by Fienup.[28] The emphasis is a critical step in the algorithm because it maintains the correlation between the current phase plate and the speckle pattern that it generates. Without this step the algorithm would diverge.

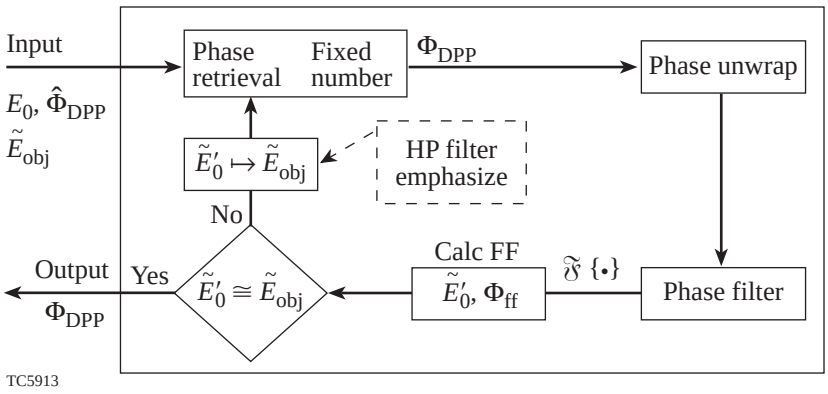

Figure 89.11
A flow diagram depicting the iterative process employed in the novel phase plate design technique and used in the code *Zhizhoo'*. Initialized near-field phase and far-field objective functions are fed into the iterative process. The standard phase-retrieval block (see Fig. 89.10) is executed first, followed by the 2-D phase unwrap and phase filter. Next, the speckled far field $\tilde{E}'_{\mathrm{obj}}\left(x_{\mathrm{ff}},y_{\mathrm{ff}}\right)$ is recalculated based on the latest unwrapped and filtered phase plate. Finally, the updated far field $\tilde{E}'_{\mathrm{obj}}\left(x_{\mathrm{ff}},y_{\mathrm{ff}}\right)$ is compared to the far-field objective $\tilde{E}_{\mathrm{obj}}\left(x_{\mathrm{ff}},y_{\mathrm{ff}}\right)$ to test for convergence and maximum number of iterations reached to determine whether or not to proceed. If proceeding, then the far-field objective functions are modified to maintain correlation with the latest iteration of the near-field phase. The modifications include a convergence enhancement, which is applied to the far-field objective. The second optional modification alters the far-field objective's power spectrum by high-pass filtering before continuing back into the standard phase-retrieval block. The dashed box denotes optional blocks.

The emphasis function requires the envelope of the far-field intensity to make these corrections. The far-field envelope is calculated using either a low-pass or an optimal filter technique.[42] The low-pass method uses a super-Gaussian filter

$$\tilde{\Psi}_{\mathrm{ff}}\left(k_{x_{\mathrm{ff}}},k_{y_{\mathrm{ff}}}\right)=\exp\left\{-\ln(2)\left(\frac{k_{\mathrm{ff}}}{2k_{\mathrm{env}}}\right)^{10}\right\}, \qquad (12)$$

where $k_{\mathrm{ff}}\equiv\left(k_{x_{\mathrm{ff}}}^2+k_{y_{\mathrm{ff}}}^2\right)^{1/2}$ is the radial wave number of the far-field coordinate system and k_{env} defines the approximate frequency where the envelope power spectrum and the speckle spectrum intersect ($k_{\mathrm{env}}=43.2\times10^3$ rad/m for OMEGA and $k_{\mathrm{env}}=5.88\times10^3$ rad/m for the NIF). The optimal filter uses the far-field power spectrum and a model of the power spectrum of the speckle:

$$\tilde{\Psi}_{\mathrm{opt}}\left(k_{x_{\mathrm{ff}}},k_{y_{\mathrm{ff}}}\right)=\frac{\left|\tilde{I}_{\mathrm{ff}}\left(k_{x_{\mathrm{ff}}},k_{y_{\mathrm{ff}}}\right)\right|^2-\Xi\left(k_{x_{\mathrm{ff}}},k_{y_{\mathrm{ff}}}\right)}{\left|\tilde{I}_{\mathrm{ff}}\left(k_{x_{\mathrm{ff}}},k_{y_{\mathrm{ff}}}\right)\right|^2}, \qquad (13)$$

where $\left|\tilde{I}_{\mathrm{ff}}\left(k_{x_{\mathrm{ff}}},k_{y_{\mathrm{ff}}}\right)\right|^2$ defines the power spectrum of the far-field intensity and $\Xi\left(k_{x_{\mathrm{ff}}},k_{y_{\mathrm{ff}}}\right)$ represents the power spectrum of the speckle intensity, which is given by the autocorrelation of the near-field intensity.[43] The optimal filter is the best method of obtaining the envelope; however, it is not compatible with the design of the high-pass phase plate because a model for the far-field power spectrum is not known for this case *a priori*. The far-field intensity envelope $I_{\mathrm{ff_{env}}}\left(x_{\mathrm{ff}},y_{\mathrm{ff}}\right)$ is calculated by applying a Fourier-filtering technique similar to Eq. (7) to the far-field intensity $I_{\mathrm{ff}}\left(x_{\mathrm{ff}},y_{\mathrm{ff}}\right)$ while using one of the filters in Eq. (12) or (13). The emphasis function may now be calculated as

$$\Lambda_{\mathrm{emp}}\left(x_{\mathrm{ff}},y_{\mathrm{ff}}\right)=\alpha\cdot\Lambda\left(x_{\mathrm{ff}},y_{\mathrm{ff}}\right), \qquad (14)$$

where $\Lambda\left(x_{\mathrm{ff}},y_{\mathrm{ff}}\right)$ is defined in Eq. (8) and α is an enhancement factor that can be used to hasten convergence by overcompensating for the distortions in the envelope function and is defined as

$$\alpha=\begin{cases}\alpha_{>1}; & \Lambda\left(x_{\mathrm{ff}},y_{\mathrm{ff}}\right)>1\\ 1\ ; & \Lambda\left(x_{\mathrm{ff}},y_{\mathrm{ff}}\right)=1\\ \alpha_{<1}; & \Lambda\left(x_{\mathrm{ff}},y_{\mathrm{ff}}\right)<1\end{cases}. \qquad (15)$$

Care must be taken in selecting the constants $\alpha_{>1}$ and $\alpha_{<1}$ because amplifying oscillations may occur that lead to loss of control and convergence failure. The values found to yield adequate convergence that avoids oscillations are $\alpha_{>1}=1.1$ and $\alpha_{<1}=0.9$. The emphasis function $\Lambda_{\mathrm{emp}}\left(x_{\mathrm{ff}},y_{\mathrm{ff}}\right)$ modifies the current far-field objective before the next trial of the standard phase-retrieval technique as

$$\tilde{E}_{\mathrm{obj}}\left(x_{\mathrm{ff}},y_{\mathrm{ff}}\right)=\Lambda_{\mathrm{emp}}\left(x_{\mathrm{ff}},y_{\mathrm{ff}}\right)\cdot\tilde{E}'_{\mathrm{obj}}\left(x_{\mathrm{ff}},y_{\mathrm{ff}}\right), \qquad (16)$$

where $\tilde{E}'_{\mathrm{obj}}\left(x_{\mathrm{ff}},y_{\mathrm{ff}}\right)$ represents the current objective and $\tilde{E}_{\mathrm{obj}}\left(x_{\mathrm{ff}},y_{\mathrm{ff}}\right)$ represents the new trial. Eventually the emphasis function decays toward unity as the continuous phase mapping converges; therefore the emphasis function is similar to a merit function. The emphasis function is 2-D, which enables *Zhizhoo'* to compensate for any azimuthal asymmetries or other distortions in the far-field intensity envelope.

The number of iterations or sets of the wrapper algorithm that are executed in *Zhizhoo'* may end when either a convergence criterion is reached or a maximum number of sets has occurred. The convergence criterion used in *Zhizhoo'* is a simple rms error of the calculated far field relative to the design specification, viz.

$$\sigma_{\mathrm{ff}}=\left\{\frac{\iint\limits_{\forall\mathrm{space}}\left[\tilde{E}'_{\mathrm{obj}}\left(x_{\mathrm{ff}},y_{\mathrm{ff}}\right)-\tilde{E}_{\mathrm{obj}}\left(x_{\mathrm{ff}},y_{\mathrm{ff}}\right)\right]^2dx_{\mathrm{ff}}dy_{\mathrm{ff}}}{\iint\limits_{\forall\mathrm{space}}\left[\tilde{E}_{\mathrm{obj}}\left(x_{\mathrm{ff}},y_{\mathrm{ff}}\right)\right]^2dx_{\mathrm{ff}}dy_{\mathrm{ff}}}\right\}^{1/2}, \qquad (17)$$

where $\tilde{E}'_{\mathrm{obj}}\left(x_{\mathrm{ff}},y_{\mathrm{ff}}\right)$ represents the objective produced by the current realization of the phase plate and $\tilde{E}_{\mathrm{obj}}\left(x_{\mathrm{ff}},y_{\mathrm{ff}}\right)$ represents the objective prior to the emphasis function modifications. At the completion of all the sets, the calculated continuous phase plate produces a speckled far-field intensity pattern whose envelope matches the objective function extremely well without any azimuthal asymmetries or distortions. In addition, the phase discontinuities or complex zeros of the near field are removed.

4. High-Pass Phase Plate

The ability to control the far-field intensity's power spectrum and produce a high-pass phase plate is merely an extension to the novel phase plate design technique; a step, which is

added to the algorithm, revises the power spectrum of the far-field objective during the iterative process. This step becomes part of the wrapper algorithm, as indicated in Fig. 89.11, and modifies the far-field objective by high-pass filtering its power spectrum. The high-pass filtering must be done as part of the wrapper algorithm because it is necessary to maintain the correlation between the speckle pattern produced by the current phase plate (i.e., after the 2-D phase unwrapping and filtering process) just as in the application of the emphasis function. The current implementation applies the high-pass filtering before the emphasis function modifications. As the continuous-phase mapping converges, it will produce a far-field intensity envelope that matches the targeted objective as well as produce speckle with dramatically reduced power in the lower-ℓ modes. The amount of power that can be removed depends on the type of filter used. A sharp-cutoff, wideband filter can achieve about a factor-of-10 reduction in the power spectrum across the whole requested band, whereas a slowly varying filter envelope can realize as much as a factor-of-100 reduction in the lowest-ℓ modes.

After 2-D phase unwrapping and filtering, the current phase-plate realization yields an intensity speckle field $\left|E'_{\text{obj}}(x_{\text{ff}}, y_{\text{ff}})\right|^2$ comprised of a unity-mean, uniformly random speckle field, which is modulated by the far-field envelope. The far-field envelope must be removed so that the high-pass filter does not affect the targeted envelope but primarily so that the high-pass filter operates directly on the random speckle field. Separating the unity mean from the uniformly random speckle field and modulating its sum by the envelope function, constructs a model for this speckle field:

$$\left|E'_{\text{obj}}(x_{\text{ff}}, y_{\text{ff}})\right|^2 = I_{\text{ff}_{\text{env}}}(x_{\text{ff}}, y_{\text{ff}})\left[1 + \text{spec}'(x_{\text{ff}}, y_{\text{ff}})\right], \quad (18)$$

where $I_{\text{ff}_{\text{env}}}(x_{\text{ff}}, y_{\text{ff}})$ is the slowly varying envelope function obtained by low-pass filtering the speckle field and $\text{spec}'(x_{\text{ff}}, y_{\text{ff}})$ is a zero-mean speckle field. The low-pass filter used to calculate $I_{\text{ff}_{\text{env}}}(x_{\text{ff}}, y_{\text{ff}})$, for this case, is given by Eq. (12) except with a super-Gaussian of order 5. The high-pass filter operates on the zero-mean speckle field $\text{spec}'(x_{\text{ff}}, y_{\text{ff}})$.

Let $E'_{\text{obj}}(x_{\text{ff}}, y_{\text{ff}})$ be the far-field objective function produced by the current realization of the phase plate after 2-D phase unwrapping and filtering, which is fed into the speckle model to yield the current zero-mean speckle field $\text{spec}'(x_{\text{ff}}, y_{\text{ff}})$. The high-pass-filtered speckle is then given by

$$\text{spec}(x_{\text{ff}}, y_{\text{ff}}) = \Re\left\{\Im^{-1}\left\{\Psi_{\text{HP}}(k_{x_{\text{ff}}}, k_{y_{\text{ff}}}) \cdot \Im\left\{\text{spec}'(x_{\text{ff}}, y_{\text{ff}})\right\}\right\}\right\}, \quad (19)$$

where $\Psi_{\text{HP}}(k_{x_{\text{ff}}}, k_{y_{\text{ff}}})$ represents any type of high-pass filter. In this article, the sharp-cutoff filter is given by

$$\Psi_{\text{HP}}(k_{x_{\text{ff}}}, k_{y_{\text{ff}}}) = \begin{cases} 1; & k_{\text{ff}} > 200/r_{\text{fuel}} \\ 0; & k_{\text{ff}} \le 200/r_{\text{fuel}} \end{cases}, \quad (20)$$

or the slowly varying filter is given by

$$\Psi_{\text{HP}}(k_{x_{\text{ff}}}, k_{y_{\text{ff}}}) = \exp\left\{-\ln(2)\left(\frac{r_{\text{fuel}} k_{\text{ff}}}{200}\right)^{2.25}\right\}, \quad (21)$$

where r_{fuel} = 500 μm is the fuel pellet radius for OMEGA. After high-pass filtering, the zero-mean speckle field is then substituted back into the speckle model to form the new far-field objective $E_{\text{obj}}(x_{\text{ff}}, y_{\text{ff}})$, viz.,

$$E_{\text{obj}}(x_{\text{ff}}, y_{\text{ff}}) = \left\{I_{\text{ff}_{\text{env}}}(x_{\text{ff}}, y_{\text{ff}})\left[1 + \text{spec}(x_{\text{ff}}, y_{\text{ff}})\right]\right\}^{0.5}. \quad (22)$$

The new far-field objective $E_{\text{obj}}(x_{\text{ff}}, y_{\text{ff}})$ would then be modified further by the emphasis function as described in the previous section.

Phase Plate Design Results

Two types of continuous phase plates were designed using *Zhizhoo'* for each laser: OMEGA and the NIF. The first type of phase plate is referred to as a standard phase plate to distinguish it from the second type, a high-pass phase plate. The standard phase plate is used as the basis of comparison to measure the ability of the high-pass phase plate to reduce the power in the lower-ℓ modes.

1. OMEGA Phase Plate Designs

The targeted far-field intensity envelope for the first OMEGA phase plate design is a super-Gaussian of order 8 (sg = 8) and an intensity-full-width-at-half-maximum (IFWHM) radius of r_0 = 432 μm:

$$I_{\mathrm{ff_{target}}}\left(x_{\mathrm{ff}}, y_{\mathrm{ff}}\right) = \exp\left\{-\ln(2)\left(\frac{r_{\mathrm{ff}}}{r_0}\right)^{\mathrm{sg}}\right\}, \quad (23)$$

where $r_{\mathrm{ff}} \equiv \left(x_{\mathrm{ff}}^2 + y_{\mathrm{ff}}^2\right)^{1/2}$ is the radius in the far-field coordinate system. This far-field intensity envelope target defines a 95% enclosed energy contour with a diameter of D_{95} = 925 μm and was chosen to demonstrate the ability of *Zhizhoo'* to produce a far-field envelope of high super-Gaussian order. The near-field clear aperture is round and has a diameter of 27.5 cm. The simulation space for the near field was a 1024 × 1024 grid spanning 55.0 cm, and the corresponding far field covered 1.18 mm on a 1024 × 1024 grid.

Zhizhoo' was run with these design parameters to calculate a continuous standard phase plate with a continuous random initial guess for the phase, which was filtered with a super-Gaussian filter of order 20 and filter cutoff parameter $k_{0_{\mathrm{DPP}}} = 360$ rad/m. The internal standard phase-retrieval code was set to run five iterations, the wrapper algorithm was set at a fixed number of 50 iterations, and emphasis was enabled. *Zhizhoo'* ran in parallel on eight processors on the SGI Origin 2000 for 15 min, which ended with a rms far-field error of σ_{ff} = 5.8%. A plot of the azimuthally averaged far-field intensity is compared to the far-field target envelope in Fig. 89.12. The agreement between the resultant far field and the target far-field envelope is excellent even for this high-order super-Gaussian. This level of agreement is achieved mainly due to the combined capabilities of the emphasis function and continuity control to keep the standard phase-retrieval method from stagnating; the error-reduction algorithm is guaranteed to never increase the error upon every iteration, and, if stagnation can be controlled, the calculated phase will converge to the correct answer with no complex zeros in the near field, i.e., no phase dislocations. These results should be compared to the relatively poor results achieved in Refs. 15, 32, and 44. The novel phase plate design technique is also able to control any azimuthal asymmetries of the far field through the application of a 2-D emphasis function. This is illustrated in Fig. 89.13 by plotting the far-field intensity contours that result from applying 1-THz, 2-D SSD and PS in the asymptotic limit.[23,24]

Zhizhoo' was then run to design both a continuous standard and high-pass phase plate with a super-Gaussian far-field target of order 3 (sg = 3) and an IFWHM radius of r_0 = 325 μm, which defines a 95% enclosed energy contour with a diameter of D_{95} = 970 μm. This super-Gaussian envelope is chosen since it produces ample uniformity on the spherical OMEGA target. The high-pass function used was a wideband, sharp filter that attempted to attenuate all modes $0 < \ell \leq 200$ and pass all others. *Zhizhoo'* completed the high-pass design in parallel in 20 min

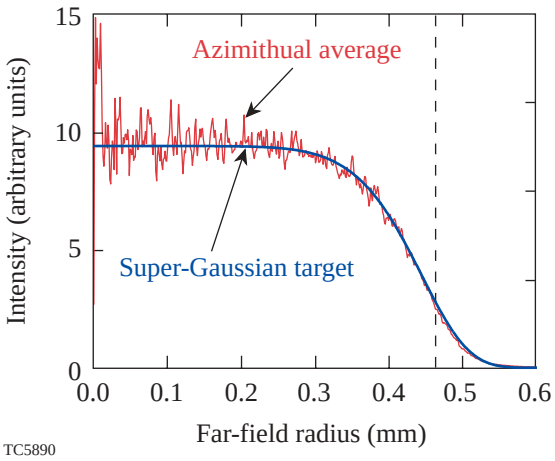

Figure 89.12
The azimuthally averaged far-field intensity (red line) is plotted against the far-field target envelope (blue line). The far-field target envelope has design parameters sg = 8 and r_0 = 432 μm. The red line is very noisy near the origin due to the limited number of points that were available to average. The dashed vertical line indicates the 95% enclosed energy contour, which is at r = 463 μm. 2-D SSD, PS, and phase aberrations are not applied.

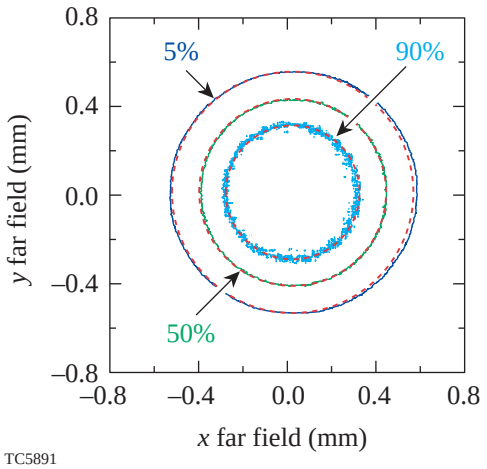

Figure 89.13
The plotted contours correspond to the 5%, 50%, and 90% of the envelope peak of the far-field intensity that result from applying 2-D SSD and PS in the asymptotic limit. The corresponding contours for the target envelope are plotted as dashed lines. The solid contours show excellent agreement to the target with very little azimuthal asymmetry. Phase aberrations have not been applied.

(it takes longer than the standard phase plate because of the additional filtering calculations) using the same fixed number of iterations as before, which ended with a rms far-field error of σ_{ff} = 5.5%; the standard phase plate design completed with σ_{ff} = 2.8%. The resultant far-field envelopes match the target function very well. The larger σ_{ff} parameter for the high-pass phase plate is due to the inability of the phase plate to reproduce the exact filtered speckle, even though the envelope is very close to the target, i.e., the objective function has less power in the low-ℓ modes compared to the resultant.

The high-pass phase plate's ability to attenuate the power spectrum in the low-order modes is illustrated in Fig. 89.14 for a single beam with and without 2-D SSD and PS. The high-pass phase plate is able to attenuate the power spectrum by a factor of ~10 over a range that doesn't include the far-field envelope $10 < \ell \le 200$. When all of the 60 OMEGA laser beams are calculated and projected onto the target sphere, the effect of the far-field envelope is removed and the high-pass phase plate is observed to attenuate the mode amplitudes over the full range $0 < \ell \le 100$ by a factor of $\sim\sqrt{10}$, as illustrated in Fig. 89.15.

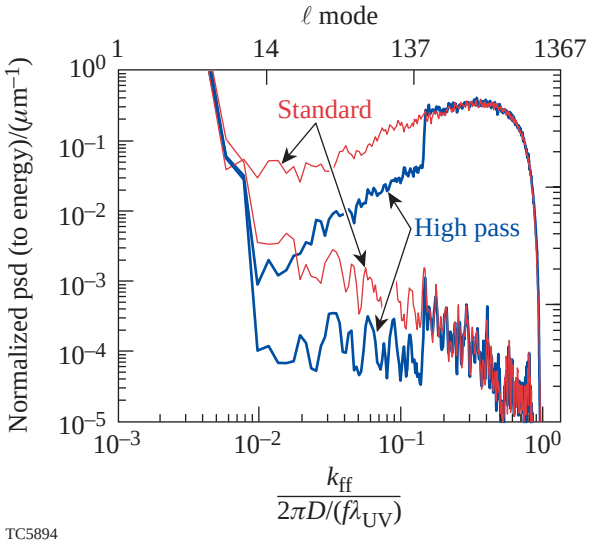

Figure 89.14
The azimuthally integrated, single-beam far-field power spectrum (normalized to the total energy) resulting from the high-pass phase plate (thick lines) for OMEGA is compared to the power spectrum of the standard phase plate (thin lines). The upper lines represent the instantaneous speckled far field without SSD or PS applied, and the lower lines represent the smoothed power spectrum that results from 1-THz, 2-D SSD with PS in the asymptotic limit. Phase aberrations have not been applied.

A second high-pass phase plate, also designed with *Zhizhoo'*, attempted to slowly reduce the far-field power spectrum over the range $0 < \ell \le 200$. The goal here was to make the greatest reduction in the lower-ℓ-mode range of $0 < \ell \le 20$. As illustrated in Fig. 89.16, the power spectrum was, on average, attenuated by nearly a full factor of 100 across the whole band $\ell < 200$ with most of the benefit occurring at the lower-ℓ modes.

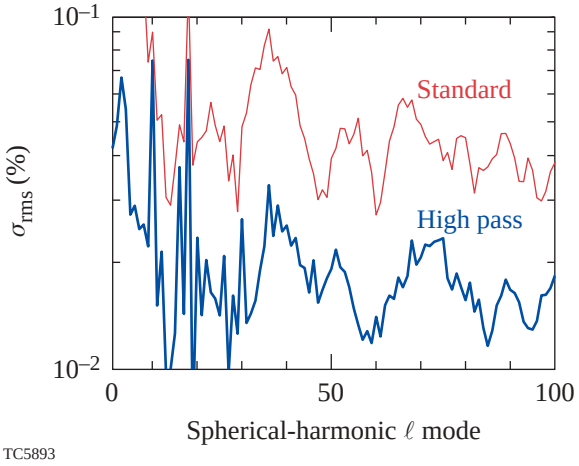

Figure 89.15
The ℓ-mode spectrum of an OMEGA 60-beam projection onto a target sphere resulting from the high-pass phase plate (blue line) is compared to the ℓ-mode spectrum of the standard phase plate (red line). These spectra result from 1-THz, 2-D SSD with PS in the asymptotic limit. The target sphere had a diameter of 950 μm. Note that these data are spectral amplitudes. The strong spectral peaks in the low-ℓ-mode range are due to the combined effect of the envelope shape and the target sphere radius, e.g., ℓ = 10.

2. NIF Phase Plate Designs

The design process for the NIF is very similar to that of OMEGA except that the near field is square and the dimensions are different. The targeted far-field intensity envelope for both NIF phase plate designs is a round super-Gaussian of order 8 (sg = 8) and an IFWHM radius of r_0 = 1.26 mm. This far-field intensity envelope target defines a 95% enclosed energy contour with a diameter of D_{95} = 2.7 mm. The higher super-Gaussian order was chosen in this case for the NIF because the faster roll-off fits better in the simulation space; a lower order would require a larger grid to provide adequate sampling of the far field (which will be done for production-quality designs). This sg = 8 still provides insight into the high-pass designs, even though it does not provide the best

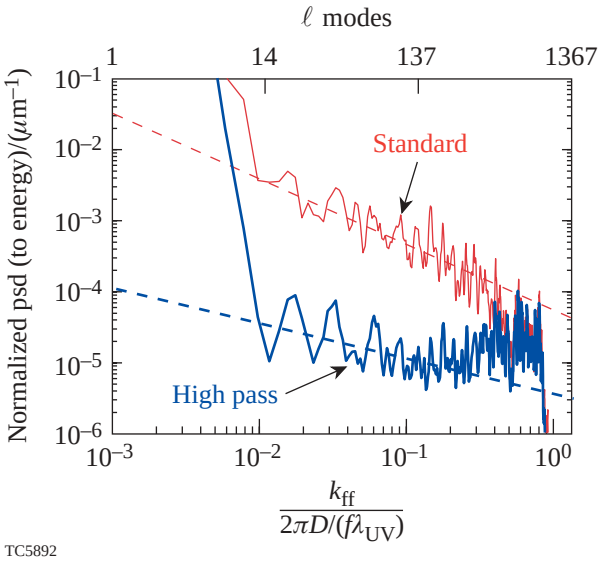

Figure 89.16
The azimuthally integrated, single-beam far-field power spectrum (normalized to the total energy) resulting from the second high-pass phase plate (blue line) is compared to the ℓ-mode spectrum of the standard phase plate (red line). These spectra result from 1-THz, 2-D SSD with PS in the asymptotic limit. The slower filter used reduced the power in the ℓ modes in the range of $0 < \ell \le 200$ by nearly a factor of 100 with most of the reduction occurring in the lower-ℓ modes. The two dashed lines represent the approximate average level of the power spectra and are intended as a guide.

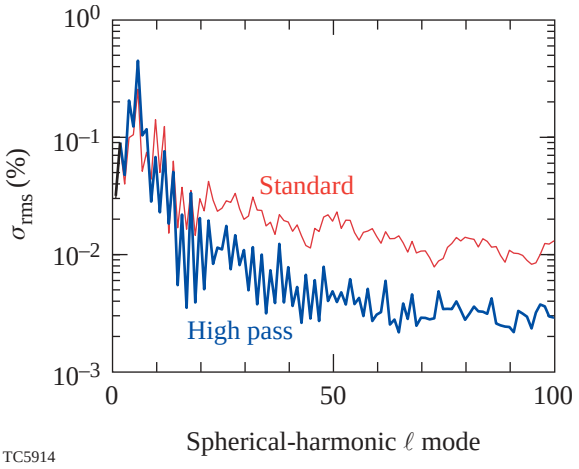

Figure 89.17
The ℓ-mode spectrum of a NIF 192-beam projection onto a target sphere resulting from the high-pass phase plate (blue line) is compared to the ℓ-mode spectrum of the standard phase plate (red line). These spectra result from 1-THz, 2-D SSD with PS in the asymptotic limit. The target sphere had a diameter of 3 mm. Note that these data are spectral amplitudes. A sharp-cutoff, wideband high-pass filter was used to attenuate the ℓ modes in the range of $0 < \ell \le 200$ and was able to reduce them by a factor of $\sim\sqrt{10}$ over this range.

spherical-target illumination. The near-field clear aperture is square and has a width of 35.1 cm in each direction. The simulation space for the near field was a 1024×1024 grid spanning 70.2 cm, and the corresponding far field covered 3.94 mm on a 1024×1024 grid.

Zhizhoo' was then run to design both a continuous standard and a high-pass phase plate to match this super-Gaussian far-field target. The high-pass function used was a wideband, sharp filter, which attempted to attenuate all modes $0 < \ell \le 200$ and pass all others. *Zhizhoo'* completed the high-pass design using the same fixed number of iterations as before, which ended with a rms near-field error of $\sigma_{ff} = 6.5\%$; the standard phase plate design completed with $\sigma_{ff} = 3.1\%$. As with the OMEGA designs, the resultant far-field envelopes match the target function very well.

Figure 89.17 illustrates the performance of the high-pass phase plate relative to the standard phase plate when all of the 192 NIF laser beams are calculated and then projected onto the target sphere. The high-pass phase plate is able to reduce the amplitudes by a factor of $\sim\sqrt{10}$ for modes over the range $0 < \ell \le 200$.

Effects of Near-Field Phase Aberrations

A near-field phase aberration can have a profound effect on the performance of the high-pass phase plates. The phase of the aberration modifies the way in which near-field elements interfere in the far field to produce the speckle pattern. The complex near field has a specific autocorrelation due to the phase pattern of the high-pass phase plate; viz., the Fourier transform of the far-field intensity is equivalent to the autocorrelation of the complex near field, i.e., the autocorrelation theorem (see Ref. 29). An aberration affects the autocorrelation of the near field and disrupts the specific relationship that was developed during the iteration process. If the aberration is strong enough, it acts like a randomizer, and the resultant far-field power spectrum tends toward that of the standard phase plate; i.e., speckle statistics that behave like those due to a phase plate with circular Gaussian statistics are simply the autocorrelation of the near-field intensity (plus a delta function at the origin).[43] If the phase aberration is not too strong, the resultant power spectrum is a hybrid of the two and lies somewhere in between.

The spatial frequency of the phase aberration affects different spatial frequencies of the far-field intensity. For example, a high-spatial-frequency phase aberration will affect the long-wavelength features in the far-field intensity and vice versa.

Since typical phase aberrations have a spatial spectrum whose spectrum follows a basic inverse power law in order that the high spatial frequencies will have less power than the lower spatial frequencies, one would expect short-wavelength features of the far-field intensity to be affected first.

The near-field phase aberration, which was measured on OMEGA, corresponds to a beam that is 12× diffraction limited. This phase aberration is used in two ways: (1) as an amplitude spectrum that is calculated and fit to an inverse power law to model phase aberrations of varying strength; and (2) as a fixed phase aberration used in *Waasikwa'* far-field simulations. The azimuthally averaged amplitude spectrum of the measured phase aberration is shown in Fig. 89.18 along with the inverse power law model, which is fit to the data. The model used to fit the azimuthally averaged amplitude spectrum of the measured near-field phase aberration is

$$\tilde{\Phi}\left(k_{\mathrm{nf}}\right) = 2\pi a\left(\frac{k_{\mathrm{nf}}}{2\pi}\right)^{b}, \tag{24}$$

where a defines the magnitude and b defines the power. For the measured near-field phase aberration, $a = 2.45$ and $b = -2.22$. It is assumed that the power law can be scaled by varying the magnitude parameter a while keeping the power b constant. In this way, different far-field simulations can be run with a varying degree of phase aberration. A measure of the strength of the phase aberration is given by the ratio

$$\beta = \frac{D_{95}}{D_{\mathrm{DL}}}, \tag{25}$$

where D_{95} is the diameter of the 95% enclosed energy contour of the far-field spot due to a phase-aberrated beam relative to the 95% enclosed energy contour for a diffraction-limited beam D_{DL}. For OMEGA the diffraction-limited far-field spot diameter is $D_{\mathrm{DL}} = 6.25\ \mu$m and, for the NIF, $D_{\mathrm{DL}} = 23.1\ \mu$m. When the parameters for the model of the power spectrum given in Eq. (24) are $a = 2.45$ and $b = -2.22$, this yields $\beta = 12$, i.e., 12× diffraction limited using the definition of Eq. (25). The phase-aberration amplitude spectrum model given in Eq. (24) can be used to generate a random phase perturbation that matches the power spectrum model, i.e., colored noise (see Ref. 41, pp. 153–154):

$$\Phi_{\mathrm{aber}}\left(x_{\mathrm{nf}}, y_{\mathrm{nf}}\right) = \Re\left\{\tilde{\mathcal{F}}^{-1}\left\{\tilde{\Phi}\left(k_{\mathrm{nf}}\right)\exp\left[i\zeta\left(k_{x_{\mathrm{nf}}}, k_{y_{\mathrm{nf}}}\right)\right]\right\}\right\}, \tag{26}$$

where $\zeta\left(k_{x_{\mathrm{nf}}}, k_{y_{\mathrm{nf}}}\right) \in [0, 2\pi]$ is a random number field and defined at Eq. (11). A random phase aberration of varying strength β can be generated using the model given by Eq. (26) by holding the power $b = -1.23$ constant and changing the value of the amplitude a.

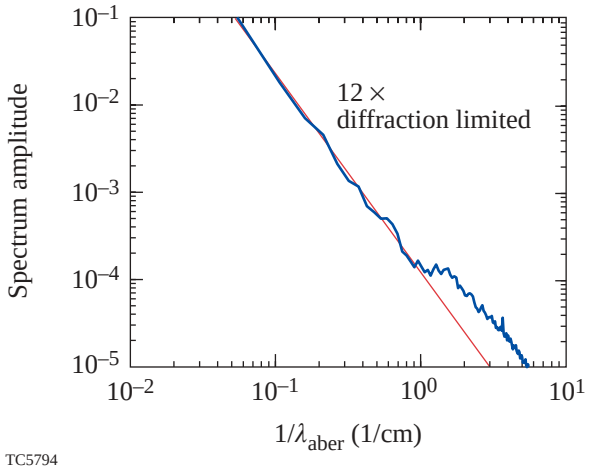

Figure 89.18
The azimuthally averaged power spectrum of a near-field phase aberration measured on OMEGA. An inverse power law model is shown as a fit to this data; fit parameters are $a = 2.4$ and $b = -2.22$ for the model in Eq. (24).

The effect that the phase-aberration strength has on the ℓ-mode spectrum of the far-field intensity for multiple-beam projections is shown in Fig. 89.19. The strength parameter β is increased, and the amplitude spectrum begins to change the shorter-wavelength features initially. This is due to the nature of the power spectrum of the phase aberration; the longer wavelengths have more power than the shorter wavelengths. The longer wavelengths of the phase aberration affect the shorter wavelengths of the far-field intensity, i.e., the autocorrelation of the complex near field is disrupted. When the strength parameter β is large enough, e.g., $\beta > 12$, it is difficult to tell the difference between the aberrated far field and the far-field intensity power spectrum due to the standard phase plate.

A benefit from the high-pass phase plates can still be realized in the lower-ℓ modes in the presence of typical near-field phase aberrations. The multiple-beam projection of the far-field intensity onto the target sphere becomes necessary to

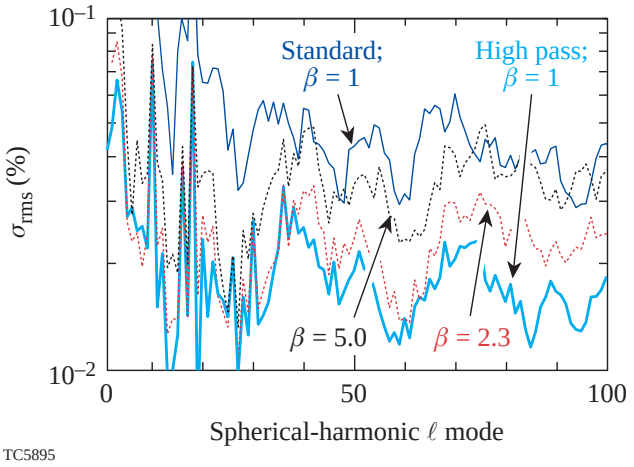

Figure 89.19
The ℓ-mode spectrum of an OMEGA 60-beam projection onto a target sphere due to the standard (upper thin line) and the high-pass (lower thick line) phase plate without phase aberrations is plotted for reference; these are the same traces that correspond to the single-beam spectra in Fig. 89.14. The ℓ-mode spectra of the far-field intensity due to the high-pass phase plate with varying degrees of phase aberration (β = 2.3 and β = 5.0) using the models in Eqs. (24) and (26) are shown (dashed lines). As the strength parameter β increases, the power spectrum tends toward that produced by the standard phase plate beginning with the shorter wavelengths. The shorter wavelengths of the far field are disrupted by the longer wavelengths of the phase aberration where the aberration has the strongest spectral amplitude (see Fig. 89.18).

gather this information because the envelope power overwhelms the power spectrum for the single beam for modes $\ell < 20$. A measure of the benefit gained from the high-pass phase plate is given by the ratio of the nonuniformity due to the high-pass phase relative to the standard phase plate summed over the desired ℓ-mode range, viz.,

$$\Gamma = \left[\frac{\sum_{\ell=\ell_{min}}^{\ell_{max}} \gamma_\ell^2}{\sum_{\ell=\ell_{min}}^{\ell_{max}} \hat{\gamma}_\ell^2} \right]^{1/2}, \qquad (27)$$

where γ_ℓ and $\hat{\gamma}_\ell$ are the amplitudes of the spherical ℓ-mode decomposition for the high-pass and standard phase plates, respectively. The amount of benefit that can be realized becomes a function of the ℓ-mode range covered because of (1) the aforementioned effect of the shape of the phase aberration power spectrum and (2) the stationary modes on the target sphere that develop from the shape of the far-field envelope.

The high-pass benefit function Γ (for the high-pass phase plate designed with the wideband sharp filter) is plotted in Fig. 89.20 for the OMEGA laser as a function of the phase-aberration strength β for four different ℓ-mode ranges. The lower-ℓ-mode range $11 \le \ell \le 25$ realizes the largest benefit (Γ = 1.6 for typical system aberration of β = 12) because the shortest-wavelength features of the phase aberration are not strong enough to totally disrupt the high-pass phase plate. The high-pass phase plate that was designed with the slower filter also achieves an $\Gamma \sim \sqrt{2}$ even though the non-aberrated performance is much higher than that of the first high-pass phase plate. The results for the NIF high-pass phase plate are very similar and are shown in Fig. 89.21. A scaled model of the near-field phase aberration is used for the NIF calculations since the actual aberration is not currently known.

As a final look at the performance of the high-pass phase plates on OMEGA, two *Waasikwa'* far-field simulations were run for a square pulse shape with 1-THz, 2-D SSD and PS: one with the standard phase plate and one with the high-pass phase plate. *Waasikwa'* has the ability to perform multiple-beam projections onto a target sphere: 60 beams are projected onto a target sphere with a diameter of 950 μm. The nonuniformity, covering the ℓ modes $12 \le \ell \le 25$, of far-field intensity due to the standard phase plate is plotted in Fig. 89.22 against that due to the high-pass phase plate. The full benefit of the high-pass phase plate is not realized until after 300 ps. This occurs

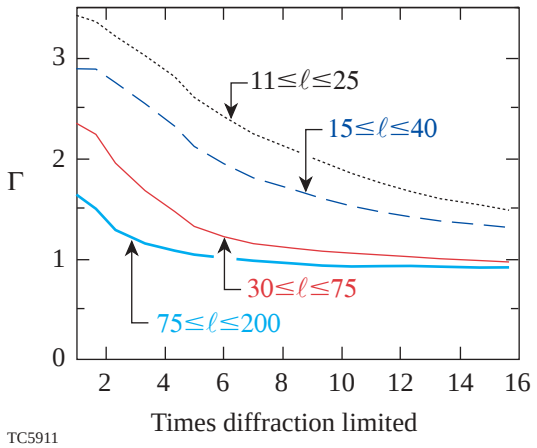

Figure 89.20
The benefit realized by the high-pass phase plate [given by Eq. (27)] is plotted as a function of the phase-aberration strength β for the OMEGA laser. The smoothing applied is 1-THz, 2-D SSD in the asymptotic limit with PS. Four different ℓ-mode ranges are covered (as labeled on the plot): $11 \le \ell \le 25$, $15 \le \ell \le 40$, $30 \le \ell \le 75$, and $75 \le \ell \le 200$.

because early in time the phase imparted by the 2-D SSD system disrupts the specific autocorrelation of the complex near field in the same way that a phase aberration does. In contrast to the static phase aberration, the phase due to 2-D SSD moves across the near field at a constant rate.[45] This movement over time effectively averages the phase due to 2-D SSD after the duration of the slowest phase modulator. In the case of the current 1-THz, 2-D SSD system, the slowest modulator is 3.3 GHz, which yields a cycle time of ~300 ps.

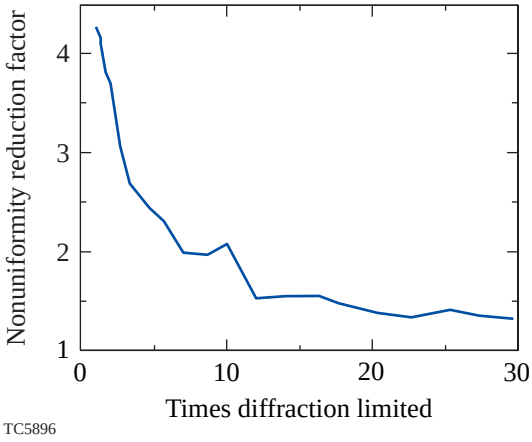

Figure 89.21
The benefit realized by the high-pass phase plate [given by Eq. (27)] is plotted as a function of the phase-aberration strength β for the NIF laser. The smoothing applied is 1-THz, 2-D SSD in the asymptotic limit with PS. A single ℓ-mode range is covered: $20 \le \ell \le 60$.

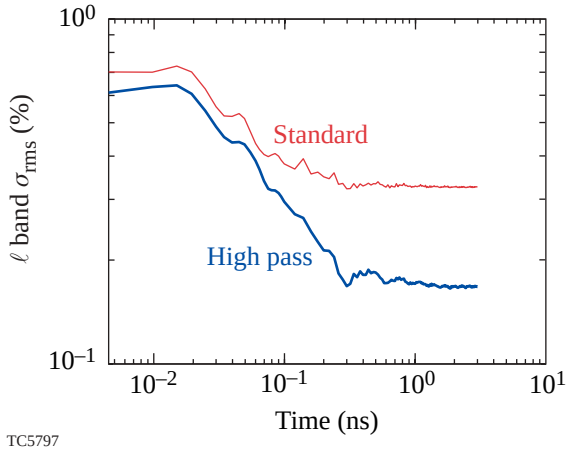

Figure 89.22
The nonuniformity of the far-field intensity over the ℓ-mode range of $12 \le \ell \le 25$ due to the standard phase plate is plotted against that due to the high-pass phase plate for the OMEGA laser. The data represent the results of *Waasikwa'* far-field simulations for a square pulse shape and 1-THz, 2-D SSD with PS. The measured near-field phase aberration was applied to both cases. The full benefit of the high-pass phase plate is not achieved until after 300 ps, when the slowest modulator (ν_m = 3.3 GHz) has completed one full cycle.

Conclusion

A novel phase plate design technique, based on the standard phase-retrieval algorithm, has been introduced and is able to generate continuous phase plates with outstanding control of the far-field intensity envelope, azimuthal asymmetries, and the far-field power spectrum. This new technique is able to overcome many of the difficulties associated with the standard phase-retrieval algorithm (namely, stagnation) and is able to capitalize on the computational efficiency of this method.

The novel phase plate design technique was incorporated into a code called *Zhizhoo'*, which is used to calculate a number of continuous phase plates for both OMEGA and the NIF. A standard phase plate was designed and employed as a reference to the high-pass phase plates in order to measure the performance when the power in the low ℓ-mode range is reduced. Without near-field phase aberrations, large benefit factors of $\Gamma \sim \sqrt{10}$ or even $\Gamma \sim 10$ are obtained, depending on the manner in which the far-field power spectrum is filtered during the iterative calculations carried out in *Zhizhoo'*. Near-field phase aberrations were shown to have a deleterious affect on the performance of the high-pass phase plates. It was found that a reasonable benefit is still realized, $\Gamma \sim 2$ for the ℓ-mode range $12 \le \ell \le 25$, even in the presence of typical near-field phase aberrations. A benefit for both OMEGA and the NIF in the lower and more-dangerous ℓ modes is anticipated by using the high-pass phase plates for direct-drive ICF experiments.

ACKNOWLEDGMENT

The author would like to thank Dr. Stan Skupsky for suggesting this project and Dr. Reuben Epstein for informative discussions. In addition, this work was partially supported by the U.S. Department of Energy Office of Inertial Confinement Fusion under Cooperative Agreement No. DE-FC03-92SF19460, the University of Rochester, and the New York State Energy Research and Development Authority. The support of DOE does not constitute an endorsement by DOE of the views expressed in this article.

REFERENCES

1. C. P. Verdon, Bull. Am. Phys. Soc. **38**, 2010 (1993).

2. S. E. Bodner, D. G. Colombant, J. H. Gardner, R. H. Lehmberg, S. P. Obenschain, L. Phillips, A. J. Schmitt, J. D. Sethian, R. L. McCrory, W. Seka, C. P. Verdon, J. P. Knauer, B. B. Afeyan, and H. T. Powell, Phys. Plasmas **5**, 1901 (1998).

3. D. K. Bradley, J. A. Delettrez, and C. P. Verdon, Phys. Rev. Lett. **68**, 2774 (1992).

4. J. Delettrez, D. K. Bradley, and C. P. Verdon, Phys. Plasmas **1**, 2342 (1994).

5. J. D. Kilkenny, S. G. Glendinning, S. W. Haan, B. A. Hammel, J. D. Lindl, D. Munro, B. A. Remington, S. V. Weber, J. P. Knauer, and C. P. Verdon, Phys. Plasmas **1**, 1379 (1994).

6. R. Epstein, J. Appl. Phys. **82**, 2123 (1997).

7. V. A. Smalyuk, T. R. Boehly, D. K. Bradley, V. N. Goncharov, J. A. Delettrez, J. P. Knauer, D. D. Meyerhofer, D. Oron, and D. Shvarts, Phys. Rev. Lett. **81**, 5342 (1998).

8. F. J. Marshall and G. R. Bennett, Rev. Sci. Instrum. **70**, 617 (1999).

9. F. J. Marshall, J. A. Delettrez, V. Yu. Glebov, R. P. J. Town, B. Yaakobi, R. L. Kremens, and M. Cable, Phys. Plasmas **7**, 1006 (2000).

10. S. Skupsky, R. W. Short, T. Kessler, R. S. Craxton, S. Letzring, and J. M. Soures, J. Appl. Phys. **66**, 3456 (1989).

11. Laboratory for Laser Energetics LLE Review **69**, 1, NTIS document No. DOE/SF/19460-152 (1996). Copies may be obtained from the National Technical Information Service, Springfield, VA 22161.

12. S. Skupsky and R. S. Craxton, Phys. Plasmas **6**, 2157 (1999).

13. J. E. Rothenberg, J. Opt. Soc. Am. B **14**, 1664 (1997).

14. T. J. Kessler, Y. Lin, J. J. Armstrong, and B. Velazquez, in *Laser Coherence Control: Technology and Applications*, edited by H. T. Powell and T. J. Kessler (SPIE, Bellingham, WA, 1993), Vol. 1870, pp. 95–104.

15. Y. Lin, T. J. Kessler, and G. N. Lawrence, Opt. Lett. **21**, 1703 (1996).

16. T. R. Boehly, D. L. Brown, R. S. Craxton, R. L. Keck, J. P. Knauer, J. H. Kelly, T. J. Kessler, S. A. Kumpan, S. J. Loucks, S. A. Letzring, F. J. Marshall, R. L. McCrory, S. F. B. Morse, W. Seka, J. M. Soures, and C. P. Verdon, Opt. Commun. **133**, 495 (1997).

17. Y. Kato, unpublished notes from work at LLE, 1984.

18. K. Tsubakimoto *et al.*, Opt. Commun. **91**, 9 (1992).

19. K. Tsubakimoto *et al.*, Opt. Commun. **103**, 185 (1993).

20. Laboratory for Laser Energetics LLE Review **45**, 1, NTIS document No. DOE/DP40200-149 (1990). Copies may be obtained from the National Technical Information Service, Springfield, VA 22161.

21. T. E. Gunderman, J.-C. Lee, T. J. Kessler, S. D. Jacobs, D. J. Smith, and S. Skupsky, in *Conference on Lasers and Electro-Optics*, Vol. 7, 1990 OSA Technical Digest Series (Optical Society of America, Washington, DC, 1990), p. 354.

22. J. E. Rothenberg, J. Appl. Phys. **87**, 3654 (2000).

23. S. P. Regan, J. A. Marozas, J. H. Kelly, T. R. Boehly, W. R. Donaldson, P. A. Jaanimagi, R. L. Keck, T. J. Kessler, D. D. Meyerhofer, W. Seka, S. Skupsky, and V. A. Smalyuk, J. Opt. Soc. Am. B **17**, 1483 (2000).

24. J. A. Marozas, S. P. Regan, J. H. Kelly, D. D. Meyerhofer, W. Seka, and S. Skupsky, J. Opt. Soc. Am. B **19**, 7 (2002).

25. R. Epstein and S. Skupsky, J. Appl. Phys. **68**, 924 (1990).

26. Inspired by Anishinaabe words *zhizhoo'* meaning "spreads someone using something" and *zhizhoo'an* "spreads something using something" just as the phase plate spreads out the diffraction-limited, far-field spot to match the far-field objective. Resource: J. D. Nichols and E. Nyholm, *A Concise Dictionary of Minnesota Ojibwe* (University of Minnesota Press, Minneapolis, 1995).

27. R. W. Gerchberg and W. O. Saxton, Optik **35**, 237 (1972).

28. J. R. Fienup, Appl. Opt. **21**, 2758 (1982).

29. J. W. Goodman, *Introduction to Fourier Optics* (McGraw-Hill, New York, 1988).

30. E. Wolf, Proc. Phys. Soc. **80**, 1269 (1962).

31. F. Wyrowski and O. Bryngdahl, J. Opt. Soc. Am. A **5**, 1058 (1988).

32. Y. Lin, T. J. Kessler, and G. N. Lawrence, Opt. Lett. **20**, 764 (1995).

33. B. Ya. Zel'dovich, N. F. Pilipetsky, and V. V. Shkunov, in *Principles of Phase Conjugation*, edited by J. M. Enoch *et al.*, Springer Series in Optical Sciences (Springer-Verlag, Berlin, 1985), Sec. 3.5, Vol. 42, pp. 79–84.

34. H. Aagedal *et al.*, J. Mod. Opt. **43**, 1409 (1996).

35. D. C. Ghiglia and M. D. Pritt, *Two-Dimensional Phase Unwrapping: Theory, Algorithms, and Software* (Wiley, New York, 1998).

36. J. R. Fienup and C. C. Wackerman, J. Opt. Soc. Am. A **3**, 1897 (1986).

37. E. C. Titchmarsh, Proc. London Math. Soc. **25**, 283 (1926).

38. M. S. Scivier and M. A. Fiddy, J. Opt. Soc. Am. A **2**, 693 (1985).

39. M. S. Scivier, T. J. Hall, and M. A. Fiddy, Opt. Acta **31**, 619 (1984).

40. N. B. Baranova and B. Ya. Zel'dovich, Sov. Phys.-JETP **53**, 925 (1981).

41. A. B. Carlson, *Communication Systems: An Introduction to Signals and Noise in Electrical Communication*, McGraw-Hill Electrical and Electronic Engineering Series (McGraw-Hill, New York, 1968), pp. 153–154.

42. W. H. Press, *Numerical Recipes in C: The Art of Scientific Computing* (Cambridge University Press, Cambridge, England, 1988).

43. J. W. Goodman, in *Laser Speckle and Related Phenomena*, edited by J. C. Dainty, Topics in Applied Physics (Springer-Verlag, Berlin, 1984), Chap. 2, Vol. 9, pp. 9–75.

44. Laboratory for Laser Energetics LLE Review **64**, 170, NTIS document No. DOE/SF/19460-99 (1995). Copies may be obtained from the National Technical Information Service, Springfield, VA 22161.

45. Laboratory for Laser Energetics LLE Review **78**, 62, NTIS document No. DOE/SF/19460-295 (1999). Copies may be obtained from the National Technical Information Service, Springfield, VA 22161.